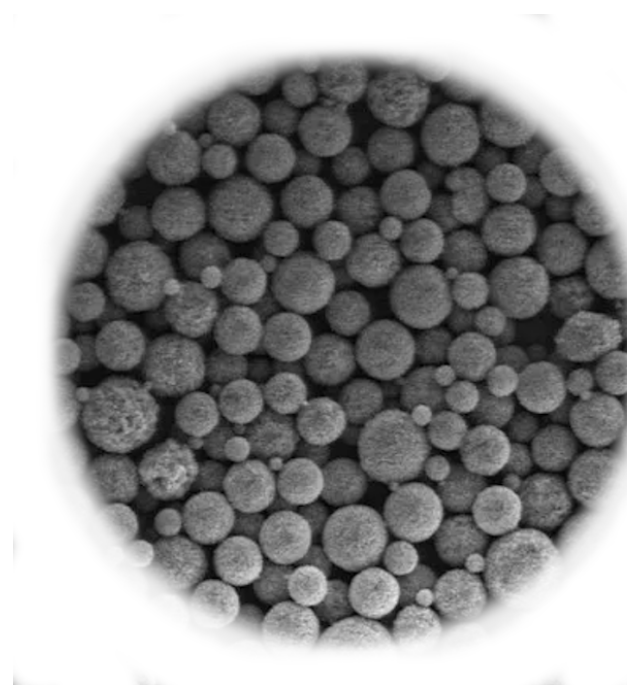


Optical Mie resonances in high-refractive-index nanostructures

Neven Gentil Supervised by Søren Raza

February to April 2022



Set Of Silicon Nanoparticles

Abstract

We propose here to pick up the Mie theory on a arbitrary nanosphere and extract the relevant cross sections. Applied to a silicon nanoparticle, we experimentally retrieve the same factors, depending on a visible range of wavelength. We finally compare them with simulated results produced from the theory and intend to give an explanation to the unmatched curves.

1 Introduction

At the nanoscale, new properties occur between nano-materials and the common visible lighting. Thereby, new technologies coupled with optical physics come to light with, for instance, shrinking light-emitting devices or color-changing surfaces. However, a precise study of scattering nanoparticles is necessary to well understand the associated phenomena. Thereby, we propose to highlight optical Mie resonances in silicon nanostructures. This type of nanoparticle is relevant in many scientific applications described before and their properties reveal the main theoretical as well as experimental basics of nano-optics.

2 Theory

The aim of this section is to develop the theoretical framework for calculating the scattering properties of a dielectric nanosphere. The results of this section will be used to simulate the scattering and extinction cross sections for comparison with the experiments. More precisely, we will mathematically represent our nanostructure and extract measurable factors from this. That said, the aim of this project is to experimentally identify the nature of the particle resonant modes and compare with those produced by scattering calculations.

2.1 Vector Spherical Harmonics

The general problem we are aiming to solve is composed of a spherical particle of radius a in background refractive medium, which is impinged by a monochromatic plane wave. With a fixed refractive index N for the nanosphere, respectively N_I for the medium and other specific parameters for electromagnetic materials like the permeability μ , our objective is to, theoretically, compute the electromagnetic field inside and outside the particle, in order to find the expression of the scattered light.

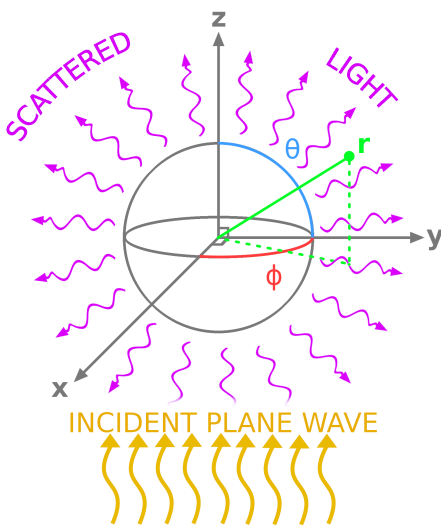


Figure 1: Diagram Of The Problem

We start with an arbitrary electromagnetic field repre-

sented by the couple of *monochromatic* vector field (\mathbf{E} , \mathbf{H}) which satisfies the Maxwell equations:

$$\nabla \cdot \mathbf{E} = 0 \quad (2.1)$$

$$\nabla \cdot \mathbf{H} = 0 \quad (2.2)$$

$$\nabla \times \mathbf{E} = i\omega\mu\mathbf{H} \quad (2.3)$$

$$\nabla \times \mathbf{H} = -i\omega\epsilon\mathbf{E} \quad (2.4)$$

Given the relation $k^2 = \omega^2\epsilon\mu$ and standards formula from vectorial analysis, we obtain a couple of *vector wave equation*:

$$\nabla^2\mathbf{E} + k^2\mathbf{E} = 0 \quad (2.5)$$

$$\nabla^2\mathbf{H} + k^2\mathbf{H} = 0 \quad (2.6)$$

where ∇^2 is the vector Laplace operator.

An important thing to notice is that any vector field with zero divergence and satisfying the vector wave equation is a valid electric/magnetic field where we can obtain the corresponding magnetic/electric field by the curl (2.3)/(2.4).

It is possible to construct a vector function \mathbf{M} depending on a scalar function ψ and an arbitrary constant vector \mathbf{c} :

$$\mathbf{M} = \nabla \times (\mathbf{c}\psi) \quad (2.7)$$

where \mathbf{M} directly satisfies the condition $\nabla \cdot \mathbf{M} = 0$. If we replace the expression of \mathbf{M} in the vector wave equation we obtain:

$$\nabla^2\mathbf{M} + k^2\mathbf{M} = \nabla \times [\mathbf{c}(\nabla^2\psi + k^2\psi)] \quad (2.8)$$

To satisfy the vector wave equation, ψ should also satisfy the equivalent scalar wave equation:

$$\nabla^2\psi + k^2\psi = 0 \quad (2.9)$$

where, this time, ∇^2 is the scalar Laplace operator. By the way, if we denote $\nabla \times \mathbf{N} = k\mathbf{M}$, we have the perpendicular vector field of the artificial \mathbf{M} , also satisfying the vector wave equation. Finally, we created the vector harmonics \mathbf{M} and \mathbf{N} with the scalar generating function ψ associated to our initial electromagnetic field.

2.2 Explicit Expansion of Vector Spherical Harmonics

The main idea to compute all solutions required is the following: given an incident electromagnetic field, we use the boundary conditions on the surface of our particle to get all fields resulting from interaction. Thereby, it could be interesting to use the spherical polar coordinates during the calculation and particularly to express the boundary conditions. That is why we have constructed the vector harmonics above. Indeed, if we replace the constant vector \mathbf{c} by the radial coordinate \mathbf{r} , \mathbf{M} is always a solution of the vector wave equation but, this time, for the spherical polar coordinates linked to the particle. In this

way, from (2.9), we obtain:

$$\begin{aligned} \frac{1}{r^2} \frac{\partial}{\partial r} \left(r^2 \frac{\partial \psi}{\partial r} \right) &+ \\ \frac{1}{r^2 \sin(\theta)} \frac{\partial}{\partial \theta} \left(\sin(\theta) \frac{\partial \psi}{\partial \theta} \right) &+ \\ \frac{1}{r^2 \sin(\theta)} \frac{\partial^2 \psi}{\partial^2 \phi} &+ \\ k^2 \psi &= 0 \end{aligned} \quad (2.10)$$

The solution to (2.10) can be obtained by using separation of the variables:

$$\psi(r, \theta, \phi) = R(r)\Theta(\theta)\Phi(\phi) \quad (2.11)$$

Upon substituting (2.11) into (2.10), we obtain three different equations, depending respectively on r , θ and ϕ which can be solved separately.

This kind of generating function ψ satisfying the scalar wave equation (2.9) is expressed in an *even* (ψ_{e}) and *odd* (ψ_{o}) function as follows:

$$\psi_{emn} = \cos(m\phi)P_n^m(\cos\theta)z_n(kr) \quad (2.12)$$

$$\psi_{omn} = \sin(m\phi)P_n^m(\cos\theta)z_n(kr) \quad (2.13)$$

where the parity of our original function is led by the *cosine* and *sine* attached with the ϕ variable and the *angle-dependent* m variable.

The other angular part described by θ , as a *Legendre's differential equation*, is solved by the *associated Legendre functions* of the first kind $P_n^m(\cos\theta)$ orthogonally defined on the n variable.

Moreover, the radial part satisfies the spherical Bessel differential equations, given by:

$$\rho \frac{d}{d\rho} (\rho \frac{dZ}{d\rho}) + [\rho^2 - (n + \frac{1}{2})^2]Z = 0 \quad (2.14)$$

where $\rho = kr$ and $Z = R(r)\sqrt{\rho(r)}$. The solution to (2.14) is any linear combination of the spherical Bessel functions j_n , y_n , $h_n^{(1)} = j_n + iy_n$ or $h_n^{(2)} = j_n - iy_n$: we named this kind of combination z_n .

We can now retrieve our initial vector spherical harmonics generated by ψ_{emn} or ψ_{omn} :

$$\mathbf{M}_{emn} = \nabla \times (\mathbf{r}\psi_{emn}) \quad (2.15)$$

$$\mathbf{M}_{omn} = \nabla \times (\mathbf{r}\psi_{omn}) \quad (2.16)$$

$$\mathbf{N}_{emn} = \frac{\nabla \times \mathbf{M}_{emn}}{k} \quad (2.17)$$

$$\mathbf{N}_{omn} = \frac{\nabla \times \mathbf{M}_{omn}}{k} \quad (2.18)$$

At this point of the theory, it is still possible to restrain our hypothesis and more precisely the shape of the incident light. Let's consider an incident plane wave given by $\mathbf{E}_i = E_0 e^{ikr \cos\theta} \mathbf{e}_r$, polarized along z-axis. Now, we can expand this wave in terms of vector spherical harmonics:

$$\begin{aligned} \mathbf{E}_i = \sum_{m=0}^{\infty} \sum_{n=m}^{\infty} B_{emn} \mathbf{M}_{emn} + B_{omn} \mathbf{M}_{omn} \\ + A_{emn} \mathbf{N}_{emn} + A_{omn} \mathbf{N}_{omn} \end{aligned} \quad (2.19)$$

where B_X and A_X are vector spherical harmonic associated factors. Thanks to the orthogonality of all the vector spherical harmonics which can be demonstrated through the properties of the functions $\cos(m\phi)$, $\sin(m\phi)$, and $P_n^m(\cos\theta)$ as well as the linear summation (2.19), we explicitly have the associated factors as follow:

$$\mathbf{B}_{emn} = \frac{\int_0^{2\pi} \int_0^{\pi} \mathbf{E}_i \cdot \mathbf{M}_{emn} \sin\theta d\theta d\phi}{\int_0^{2\pi} \int_0^{\pi} |\mathbf{M}_{emn}|^2 \sin\theta d\theta d\phi} \quad (2.20)$$

with here, for instance, the first coefficient. With the orthogonality of the sine and cosine and (2.20), we can also demonstrate that B_{emn} and A_{omn} vanish for all m and n . Then, for the same reason, B_{omn} and A_{emn} are nonzero only for $m = 1$. Moreover, regarding their behavior and our physical assumptions, we can select the spherical Bessel function replacing z_n : we choose j_n for its finite values close to $r = 0$ and denote it as ⁽¹⁾ for the associated vector spherical harmonics. Finally, we obtain:

$$\mathbf{E}_i = \sum_{n=1}^{\infty} B_{o1n} \mathbf{M}_{o1n}^{(1)} + A_{e1n} \mathbf{N}_{e1n}^{(1)} \quad (2.21)$$

Thanks to a set of properties from the associated Legendre functions, we deduce explicitly these two remaining factors B_{o1n} and A_{e1n} from (2.20) or the equivalent expression:

$$\mathbf{E}_i = E_0 \sum_{n=1}^{\infty} i^n \frac{2n+1}{n(n+1)} (\mathbf{M}_{o1n}^{(1)} - i\mathbf{N}_{e1n}^{(1)}) \quad (2.22)$$

2.3 Boundary Conditions

We have enough equation relative to the incident plane wave to apply the following boundary conditions:

$$(\mathbf{E}_i + \mathbf{E}_s - \mathbf{E}_I) \times \mathbf{e}_r = 0 \quad (2.23)$$

$$(\mathbf{H}_i + \mathbf{H}_s - \mathbf{H}_I) \times \mathbf{e}_r = 0 \quad (2.24)$$

where $(\mathbf{E}_s, \mathbf{H}_s)$ and $(\mathbf{E}_I, \mathbf{H}_I)$ are the scattered and internal electromagnetic field, respectively, resulting from the interaction between the incident field and our particle. Then, we assume that these last fields have the same mathematical shape, when developed in vector spherical harmonics, than $(\mathbf{E}_i, \mathbf{H}_i)$; that is to say, the scattering and internal field are linearly dependent from the incident field up to some factors taking into account the behavior of j_n at the boundary of our particle:

$$\mathbf{E}_I = \sum_{n=1}^{\infty} E_n (c_n \mathbf{M}_{o1n}^{(1)} - id_n \mathbf{N}_{e1n}^{(1)}) \quad (2.25)$$

$$\mathbf{H}_I = \frac{-k_I}{\omega\mu_I} \sum_{n=1}^{\infty} E_n (d_n \mathbf{M}_{e1n}^{(1)} + ic_n \mathbf{N}_{o1n}^{(1)}) \quad (2.26)$$

$$\mathbf{E}_s = \sum_{n=1}^{\infty} E_n (ia_n \mathbf{N}_{e1n}^{(3)} - b_n \mathbf{M}_{o1n}^{(3)}) \quad (2.27)$$

$$\mathbf{H}_s = \frac{k}{\omega\mu} \sum_{n=1}^{\infty} E_n (ib_n \mathbf{N}_{o1n}^{(3)} + a_n \mathbf{M}_{e1n}^{(3)}) \quad (2.28)$$

Note that ⁽³⁾ means we use the spherical Bessel function of the third kind $h_n^{(1)}$ and \mathbf{H}_X has the same factors than \mathbf{E}_X due to the curl (2.3). Moreover, k_I and μ_I are respectively the wave vector and the permeability of the particle.

Now, we can rewrite the boundary conditions on the surface of our theoretical particle from (2.23) with each component separated, that is to say at $r = a$:

$$\begin{aligned} E_{i\theta} + E_{s\theta} &= E_{I\theta} \\ E_{i\phi} + E_{s\phi} &= E_{I\phi} \\ H_{i\theta} + H_{s\theta} &= H_{I\theta} \\ H_{i\phi} + H_{s\phi} &= H_{I\phi} \end{aligned} \quad (2.29)$$

where E_{iX} , for instance, denotes the X -component of \mathbf{E}_i . We obtain four linear equations revealing the four vector spherical harmonic associated factors from $(\mathbf{E}_i, \mathbf{H}_i)$ also set into $(\mathbf{E}_I, \mathbf{H}_I)$ and $(\mathbf{E}_s, \mathbf{H}_s)$:

$$\begin{aligned} j_n(mx)c_n + h_n^{(1)}(x)b_n &= j_n(x) \\ \mu[mxj_n(mx)]'c_n + \mu_I[xh_n(x)]'b_n &= \mu_I[xj_n(x)]' \\ \mu m j_n(mx)d_n + \mu_I h_n^{(1)}(x)a_n &= \mu_I j_n(x) \\ [mxj_n(mx)]'d_n + m[xh_n^{(1)}(x)]'a_n &= m[xj_n(x)]' \end{aligned} \quad (2.30)$$

where the prime sign means derivation with respect to the argument in the parenthesis. Moreover, we have the following definitions:

$$x = ka = \frac{2\pi Na}{\lambda} \quad m = \frac{N}{N_I} \quad (2.31)$$

We solve (2.30) using Gaussian elimination to extract each coefficient. Then, as described in the next part *Cross Sections*, our wished factors are only dependent on a_n and b_n . Furthermore, these two factors could be simplified by introducing the *Riccati-Bessel* functions:

$$\psi_n(\rho) = \rho j_n(\rho) \quad \xi_n(\rho) = \rho h_n^{(1)}(\rho) \quad (2.32)$$

and we finally obtain the following expressions for the two first coefficients:

$$\begin{aligned} a_n &= \frac{m\psi_n(mx)\psi'_n(x) - \psi_n(x)\psi'_n(mx)}{m\psi_n(mx)\xi'_n(x) - \xi_n(x)\psi'_n(mx)} \\ b_n &= \frac{\psi_n(mx)\psi'_n(x) - m\psi_n(x)\psi'_n(mx)}{\psi_n(mx)\xi'_n(x) - m\xi_n(x)\psi'_n(mx)} \end{aligned} \quad (2.33)$$

Therefore, we can explicitly write the vector spherical harmonic expansions $(\mathbf{E}_s, \mathbf{H}_s)$ in order to theoretically retrieve some measurable quantities.

2.4 Cross Sections

From now on, we have enough theory to think about the experimental approach and fit all our requirements. As we can see on figure (1), this reference frame is standard in most physical areas, and our incoming plane wave is propagating along the z-axis. Thereby, our goal is currently is to calculate the net rate at which electromagnetic field crosses the surface A of an arbitrary sphere, which might be expressed as follow:

$$W = \int_A \mathbf{S} \cdot \mathbf{e}_r dA \quad (2.34)$$

where \mathbf{S} is the *Pointing vector* defined as:

$$\mathbf{S} = \frac{1}{2} \Re \{ \mathbf{E}^* \times \mathbf{H} \} \quad (2.35)$$

We can now compute this power for the scattered electromagnetic field $(\mathbf{E}_s, \mathbf{H}_s)$ which might be calculated thanks to (2.33) included into the expression of the scattered field then, after a bit of mathematical manipulations, we have a literal expression for W_s (see [CD83]). Moreover this power could be *normalized*, that is to say, divided by the intensity from the incident light. Thereby, we introduce the cross section:

$$C_{sca} = \frac{W_s}{I_i} = \frac{2\pi}{k^2} \sum_{n=1}^{\infty} (2n+1)(|a_n|^2 + |b_n|^2) \quad (2.36)$$

In the same way, all of these previous step from used to calculate W_s might be re-used for any other fields instead of the field $(\mathbf{E}_s, \mathbf{H}_s)$. Until now, only the light scattered by the particle was studied thanks to three fields: $(\mathbf{E}_i, \mathbf{H}_i)$, $(\mathbf{E}_s, \mathbf{H}_s)$ and $(\mathbf{E}_I, \mathbf{H}_I)$. However, it is possible to express a variable of extinction, opposed to the scattering *power* W_s , due to the interaction between the electromagnetic plane wave and our particle:

$$W_{ext} = W_s + W_a \quad (2.37)$$

This additional term, combined with the *absorbed power* W_a , should be easily understood through a *power balance*, that is to say an energy balance replaced by the equivalent power. Indeed, if we denote W_a the amount of power which was varying during the interaction ($W_a > 0$ means that power is absorbed within the particle), it might be possible to write the following:

$$W_a = W_i - W_s + W_{ext} \quad (2.38)$$

As our background medium is nonabsorbing, the *incident power* W_i vanishes identically and we retrieve the relation (2.37). Now, the extinction *power* can be determined using our previous vector spherical harmonic terms:

$$\begin{aligned} W_{ext} &= \frac{1}{2} \int_{\phi=0}^{2\pi} \int_{\theta=0}^{\pi} (\Re \{ E_{i\phi} H_{s\theta}^* - E_{i\theta} H_{s\phi}^* \} + \\ &\quad \Re \{ E_{s\phi} H_{i\theta}^* - E_{s\theta} H_{i\phi}^* \}) \\ &\quad r^2 \sin \theta d\theta d\phi \end{aligned} \quad (2.39)$$

and, as stated above in (2.36), we finally obtain the extinction cross section when dividing by the incident light intensity:

$$C_{ext} = \frac{W_{ext}}{I_i} = \frac{2\pi}{k^2} \sum_{n=1}^{\infty} (2n+1) \Re \{ a_n + b_n \} \quad (2.40)$$

At last, we have calculated and theoretically established the expression of two general terms which are closely related to the spectrum we measure experimentally: C_{sca} and C_{ext} . It is important to note that these cross section are, not only dependent on, but also strongly linked to our starting assumptions, that is to say our input variables like the radius a or the refractive index N . Thereby, C_{sca} and C_{ext} are directly reliant on the size of our studied particle.

3 Simulations

3.1 Equations Adjustment

Our main issue to numerically compute the cross sections C_{sca} and C_{ext} is to calculate the associated scattering coefficients a_n and b_n . Globally, these two numbers are obtained through Bessel functions as we can see from (2.33) and our goal is to retrieve each value of them between a certain range of wavelength in order to obtain the spectrum. However, due to the size of our nanoparticle close to the incident wavelength included in a visible range, the variable $\rho = kr$, as a dependency for the Bessel functions, is also restrained into a small range of value close to zero along the x-axis. In fact, in the context of a computer, these targeted values could be too sensitive to be calculated with a reasonably high precision. Thereby, we could introduce the *logarithmic derivative*:

$$D_n(\rho) = \frac{d}{d\rho} \ln[\psi_n(\rho)] \quad (3.1)$$

Thanks to this additional definition, we are expanding the range of hit values and decreasing the sensitivity. In this way, we can rearrange the expressions of a_n and b_n from (2.33):

$$\begin{aligned} a_n &= \frac{[D_n(mx)/m + n/x]\psi_n(x) - \psi_{n-1}(x)}{[D_n(mx)/m + n/x]\xi_n(x) - \xi_{n-1}(x)} \\ b_n &= \frac{[mD_n(mx) + n/x]\psi_n(x) - \psi_{n-1}(x)}{[mD_n(mx) + n/x]\xi_n(x) - \xi_{n-1}(x)} \end{aligned} \quad (3.2)$$

where we have used the recurrence relation:

$$z_n'(x) = z_{n-1}(x) - \frac{n z_n(x)}{x} \quad (3.3)$$

with z_n replaced by ψ_n or ξ_n . Note that x is not a constant because of its dependency through the wavelength λ . Moreover, due to the recurrence relations of Bessel functions explained below, in the next subsection, D_n also satisfies the following relation:

$$D_{n-1}(\rho) = \frac{n}{\rho} - \frac{1}{D_n(\rho) + n/\rho} \quad (3.4)$$

Because of the link existing between D_n and Bessel functions, this previous recurrence (3.4) should be runned downwardly, that is to say begining with the higher n owned by the scattering coefficients, in order to avoid the unstability of our computation as stated in the subsection below. Otherwise, the calculated data could be rapidly flawed while n is increasing.

3.2 Computation of Bessel Functions

Then, our last issue is to numerically compute the spherical Bessel functions, as the first, second and the associated Hankel functions or even the Riccati-Bessel functions. Hopefully, in our preferred scientific language that is *Python*, all of these features are already implemented. However, it could be interesting to speed up the computation thanks to a low-level programming language, or

more generally, a compiled one. At least, for a better understanding of the computation, we can define a way to numerically implement these tools.

To contextually replace our problem, these Bessel functions are introduced in our theory through the resolution of the radial part (2.14) in order to get a global expression of the generating couple of function ψ_{emn} and ψ_{omn} . Involving spherical coordinates in our calculation, we must use the spherical Bessel functions j_n and y_n which are a special case of general Bessel functions J_n and Y_n solving the Bessel's differential equation:

$$x^2 \frac{d^2 y}{dx^2} + x \frac{dy}{dx} + (x^2 - \alpha^2)y = 0 \quad (3.5)$$

where α is a complex number without restriction. Thereby, we have the following definitions:

$$j_n(x) = \sqrt{\frac{\pi}{2x}} J_{n+\frac{1}{2}}(x) \quad y_n(x) = \sqrt{\frac{\pi}{2x}} Y_{n+\frac{1}{2}}(x) \quad (3.6)$$

Note that the actual x might be real or a complex value and is, by definition, different from all previous sections.

After some mathematics calculation, it is possible to demonstrate the following recurrence relations:

$$\frac{2n+1}{x} z_n(x) = z_{n-1}(x) + z_{n+1}(x) \quad (3.7)$$

$$(2n+1) \frac{d}{dx} z_n(x) = nz_{n-1}(x) - (n+1)z_{n+1}(x) \quad (3.8)$$

where z_n is either j_n or y_n . Thanks to these previous equations (3.7), and given the two first exact expression for the spherical Bessel functions, we can theoretically obtain all wished order n . So, *by hand*, we have the following:

$$\begin{aligned} j_0(x) &= \frac{\sin(x)}{x} & j_1(x) &= \frac{\sin(x)}{x^2} - \frac{\cos(x)}{x} \\ y_0(x) &= -\frac{\cos(x)}{x} & y_1(x) &= -\frac{\cos(x)}{x^2} - \frac{\sin(x)}{x} \end{aligned} \quad (3.9)$$

Thereby, by inverting the main recurrence relations (3.7) into this way:

$$z_{n+1}(x) = \frac{2n+1}{x} z_n(x) - z_{n-1}(x) \quad (3.10)$$

we should be able to compute the next order $n = 2$ for a given x either real or complex. Continuing with the same idea, we can obtain $j_3, j_4\dots$ coupled with the associated y_n . This way to compute all wished spherical Bessel function, or more generally any function recursively defined, from the lowest order $n = 0$ reaching the highest order $n = \infty$, is commonly called an *upward recurrence*. Assuming that we have in our possession a couple of spherical Bessel function at the order $n = i$ and $n = i + 1$, an opposed computation from the previous one, should allow us to recursively reach $n = 0$:

$$z_{n-1}(x) = \frac{2n+1}{x} z_n(x) - z_{n+1}(x) \quad (3.11)$$

that is called a *downward recurrence* because of the decrement of n for each calculated value. Despite these two recursive ways are strictly equivalent from a mathematical

point of view, there is a not negligible difference between them. Indeed, taking into account boundaries of coding number (currently 64 bit for a common *float*) and the behavior of spherical Bessel functions, it is possible, but tough, to demonstrate either the stability or the instability for the first and second kind calculated through downward or upward recurrence. Otherwise, by a *hand* way, we can easily retrieve these theoretical results by comparing our calculations with exact curves already tabulated:

- Stable by **upward** recurrence:

$$\begin{aligned} * & y_n, \forall x \\ * & j_n, \text{ if } |x| \geq n \end{aligned}$$

- Stable by **downward** recurrence:

$$* j_n, \text{ if } |x| < n$$

assuming that $\Re\{x\} \in \mathbb{R}_+$. Now, we can think about the programming steps in order to compute our spherical Bessel functions of the first and second kind through an upward recurrence: we get j_0/y_0 and j_1/y_1 from a given x then, thanks to (3.10), we compute all required order j_n/y_n with $n \geq 2$. However, a question remains in a downward recurrence: How to get starting Bessel function values for higher order $n = i$ and $n = i + 1$?

Theoretically, it is well known that Bessel functions of the first kind J_n satisfies the following relation:

$$\forall x \mid \Re\{x\} \in \mathbb{R}_+, \lim_{n \rightarrow \infty} J_n(x) = 0 \quad (3.12)$$

Thereby a common approach, called the *Miller* method, is to suppose that our targeted higher order i is arbitrarily equal to 1 whereas the $i + 1$ order is null. Afterward, we can easily pull down the order thanks to (3.11). Once we obtain the first order $n = 0$, because of the linearity of our recurrence relations, we *normalize* this serie by the true value of $j_0(x)$.

For example:

$$\begin{aligned} j_{i+1}^{\text{computed}}(x) &= 0 \\ j_i^{\text{computed}}(x) &= 1 \\ j_{i-1}^{\text{computed}}(x) &= \frac{2i+1}{x} j_i^{\text{computed}}(x) - j_{i+1}^{\text{computed}} \quad (3.13) \\ &\dots \\ j_0^{\text{computed}}(x) &= \alpha \end{aligned}$$

Now, we can *normalize*:

$$\begin{aligned} j_0(x) &= \frac{\sin(x)}{x} \quad (\text{by definition}) \\ j_0^{\text{final}}(x) &= j_0^{\text{computed}}(x) \times \frac{j_0(x)}{\alpha} = j_0(x) \\ j_1^{\text{final}}(x) &= j_1^{\text{computed}}(x) \times \frac{j_0(x)}{\alpha} \quad (3.14) \\ &\dots \\ j_i^{\text{final}}(x) &= j_i^{\text{computed}}(x) \times \frac{j_0(x)}{\alpha} \end{aligned}$$

where j_X^{final} is the wished result. In fact, we just have *normalized* our serie j_X^{computed} by the initial factor $\frac{j_0(x)}{\alpha}$.

It is important to notice that any serie constructed through this way always verifies the recurrence relation (3.10) and each term is, by definition, a solution of the radial part (2.14).

Unfortunately, a last issue still remains in our downward recurrence approach. Something that is not obvious at the first glance, we see for a given i and any x (still with the condition $|x| < i$), due to the mathematical shape of our recurrence relation (3.11), each value of a lower computed order is bigger than its previous higher order: $j_0^{\text{computed}} > j_1^{\text{computed}} > \dots > j_i^{\text{computed}}$. So, if we target a really high order with, for instance, $i = 10^{10}$, the first order will ineluctably get a really high value before the *normalization*. Thereby, for a computer with *physical* boundaries for its numbers, this previous result will give us an invalid value for an intermediate order and all order below will be saturated with the same invalid state. In this way, the *normalization* step is impossible because α in (3.14) will own a *Nan* value (that is a computer overflow indicator). Even if, for a first approximation, we use the ten first order for calculation, this phenomenon will be rapidly visible even for our range of value (from $n = 50$) and it could be interesting to avoid this *blocking* state showed on figure (2). Note that zero values into

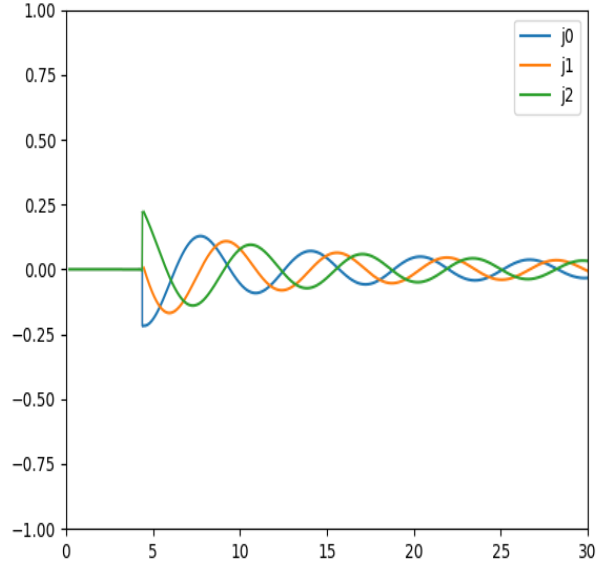


Figure 2: Downward Recurrence bug For $n = 60$

$x = [0, 4]$ is due to the invalid state. This specific *bugged* range is increasing if n also increase: the *real* dependency on x of the downward recurrence relation (3.11) is visible here.

Therefore, the first solution proposed in many other articles treating the *Mie Theorie*, or more generally the computation of Bessel functions, is to set an arbitrary minimal value for i , that is to say 10^{-10} instead of 1. However, this method will only postpone the phenomenon and allow to compute for $i = 100$ in our case. A second solution is proposed by *Liang-Wu* in [Lia10]. In a more

simple way, the idea is to divide the downward recurrence into multiple chunks. In fact, if we want $i = 1000$ as a final order, we can calculate $j_X^{computed}$ from $n = 0$ to $n = 50$ (stability limit for 64-bit numbers) and apply a normalization as previously stated for this first chunk. Secondly, we compute a second chunk starting from $n = 50$ to $n = 100$ (actually, the computation begins with $n = 100$ because of the downward behavior). It is important to notice that $\{j_{50}^{computed}, \dots, j_{100}^{computed}\}$ is larger term by term from $\{j_0^{computed}, \dots, j_{50}^{computed}\}$ due to the n dependency included into the recurrence relation but much less sensitive to the overflowing effect. For the second chunk, we can normalize it by $j_{50}^{computed}$ from the first chunk, itself normalized by the exact $j_0(x)$. This method is chain-shaped and we recursively advance, chunk by chunk to finally obtain much more wished order without overflowing the computer results as viewed on figure (2).

3.3 Input Variables

At this point of our simulation part, we have to precisely fix and set our input variables, that is to say with, roughly, this following pattern:

$$Output = Simulation(Input) \quad (3.15)$$

where *Output* is our wished scattering and extinction cross sections. Given the relations (2.36) and (2.40) coupled with the expressions of a_n and b_n previously established, we are able to recognize these variables. Thereby, all inputs are included into (2.31) with refractive indices of the medium N_I and the particle N , the particle's size a then the wavelength λ .

Let's consider the λ variable. The problem is the following: from our theory, we send an incident monochromatic light, that is to say $\lambda = constant$ in the visible range. However, in reality, the experimental tool produce multiple monochromatic lights in order to reach all values in the visible range and compute the associated cross sections. In fact, the wavelength λ will vary for each computation and, by the way, is an *Input* variable. Therefore, we have $x = x(\lambda)$ and more precisely $k = k(\lambda)$

The particle's size a represents the radius of this last one. For the purpose of this study, it is also an *Input* variable.

The refractive index of the background, taking into account that the environment is homogenous, this last one is a constant value. Even more, if we consider that the medium is the ambient air, it might be possible to approximate it as the void and finally set $N_I = 1$. Moreover, we have now the following relation $m = N$.

The last variable to describe is the refractive index N of our particle. At this point, we can introduce the targeted material, that is to say, the substance used into our spherical sample: silicon. As a first approximation, we can say that silicon has a constant refractive index commonly setted around 3.5. Thereby, for $a = 100$ nm and $\lambda = [206nm, 826nm]$ (visible range a bit extended in the *UV* range), we obtain the following cross sections: where *Sca* is the scattering, *Ext* the extinction and *Abs* the absorbtion cross section linked with (2.37):

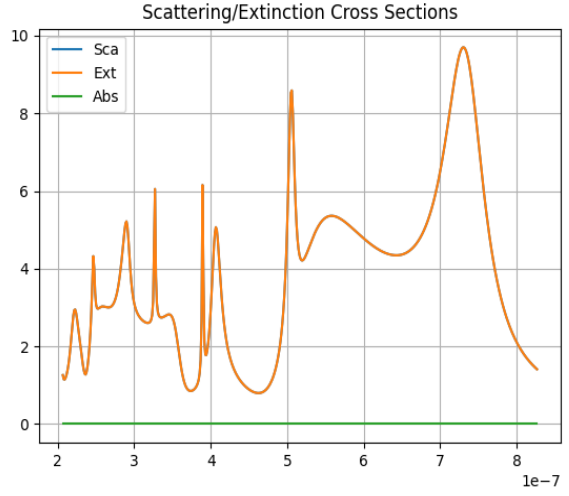


Figure 3: Extinction, scattering, and absorption cross section for a constant refractive index $N = 3.5$. Note that the scattering and extinction cross sections are identical as there is no absorption.

$C_{abs} = C_{ext} - C_{sca}$. We can see on figure (3) that there is no absorbtion and the scattering cross section equals the extinction one. However, to properly describe physical states of matter, we have to consider that the refractive index is varying depending on the wavelength of the incident light, that is to say, $N = N(\lambda)$. In this way we obtain: where we use the real part of measured refractive

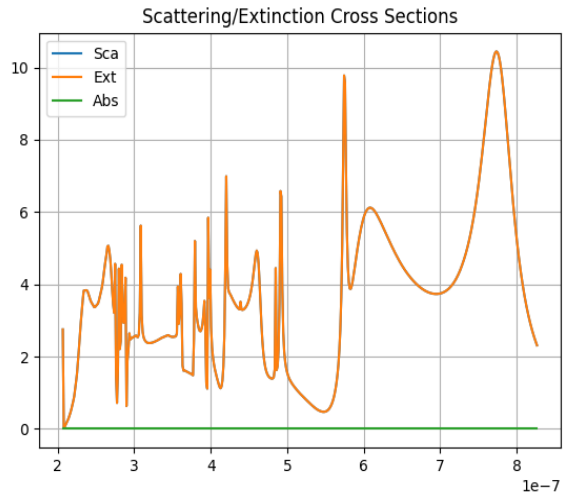


Figure 4: Extinction, scattering, and absorption cross section for wavelength-dependent and real-valued refractive index

indices from another scientific experiment (Aspnes and Studna, 1983). We easily see that the main maximum, called *Mie resonances*, are shifted to the right because of the higher value of the refractive index $N > 3.5$, but this approach globally keep the previous shape. It is always remarkable that $C_{sca} = C_{ext}$. That is due to the real expression of the refractive index. Indeed, the absorbtion

behavior of our material is mathematically implemented through the imaginary part of N . In this way, we should have $N = N_{re} + iN_{im}$. Thereby, when we use a complex varying index, we obtain: Now, in addition to the previous

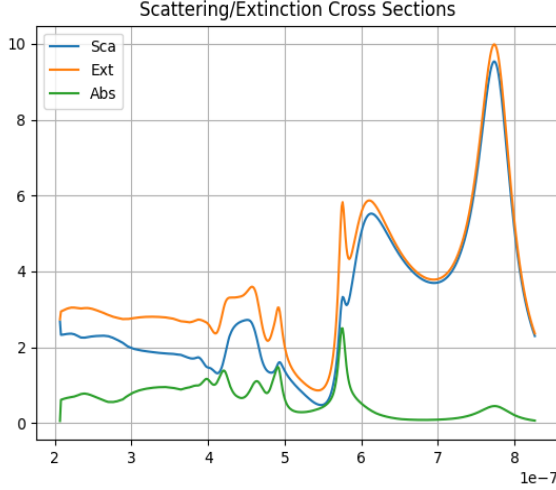


Figure 5: Extinction, scattering, and absorption cross section for wavelength-dependent and complex refractive index

ous shape then according to each Mie's resonance peak, we have a maximum of absorption describing the capacity of our particle to redistribute the energy of the incident light into another form, like a thermal energy. It is important to notice that the varying imaginary part can slightly change the position of the peak if it is high enough.

Finally, our *Input* variables are the following: a (particle's size), λ (incident light's wavelength) and $N(\lambda)$ (refractive index depending on λ).

3.4 Results

We are now in a position to compute our required *Output* which are the scattering C_{sca} and extinction C_{ext} cross sections. As a reminder and as stated in the end of the *theory* part, these last are relevant in the study of nanoparticles because cross sections are directly linked to the scattering measurements.

First at all, it could be interesting to visualize the different contributions of each terms in cross section expressions (2.36) and (2.40). Indeed, these two relations are primarily composed of an infinite sum which might be *separated* in order to compute the associated a_n and b_n terms roughly as following:

$$\sum_{n=1}^{\infty} f_n(a_n) + f_n(b_n) = \sum_{n=1}^{\infty} f_n(a_n) + \sum_{n=1}^{\infty} f_n(b_n) \quad (3.16)$$

where $f_n(X) = \frac{2\pi}{k^2}(2n+1)\Re\{X\}$ in the case of C_{ext} (with a similar expression for C_{sca}). In this way, for an arbitrary particle defined by a radius of 100 nm meters, we obtain figures (6) then (7) for the scattering and extinction cross section respectively. These figures show that each local maximum is due to a heavy weighting from one or the

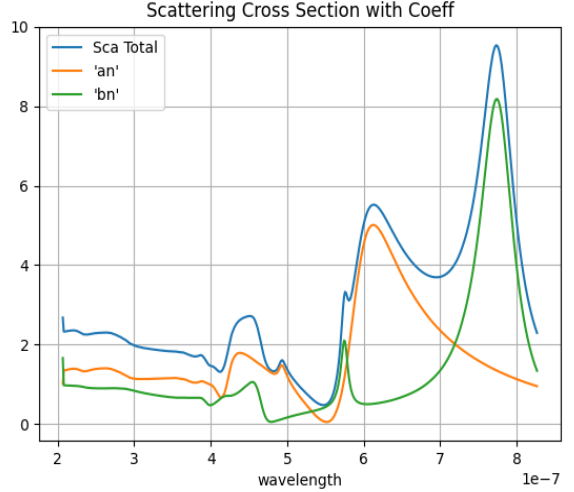


Figure 6: C_{sca} Coefficient Contributions

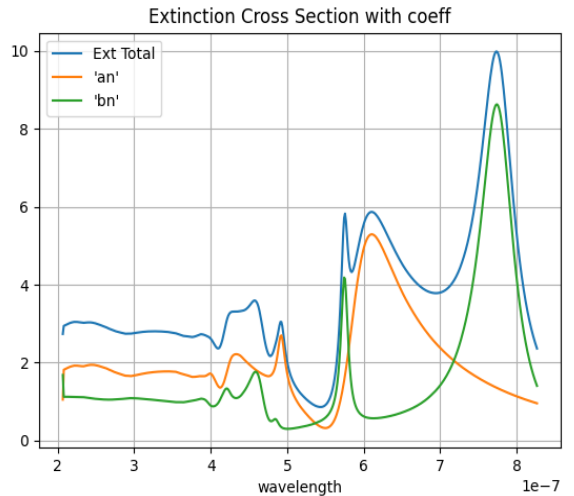


Figure 7: C_{ext} Coefficient Contributions

other of the coefficients. More particularly, the global maximum called *first magnetic dipole mode* seems to be generated by the second coefficient b_n whereas the first one, a_n influences the second global maximum which is located on the left of the first maximum.

Secondly, as stated in the previous subsection, we have three *Input* variables that we can potentially change. Note that the incident light's wavelength is fixed by the targeted range of value for the *extended-visible* light and the refractive index of our particle, depending on λ , is fixed by the material studied: silicon. Thereby, our last *free* parameter is the size or more precisely the radius. Therefore, when varying this *Input* variable, we obtain figures (8) and (9) associated to C_{sca} and C_{ext} for three different sizes surrounding all possible particles encountered during the experiments. As we can see, it is possible to consider a *recursive* shape which is composed by the boundary of the first and second global maximum. In fact, the first magnetic dipole mode is moving to lower wavelengths when the size decreases and recip-

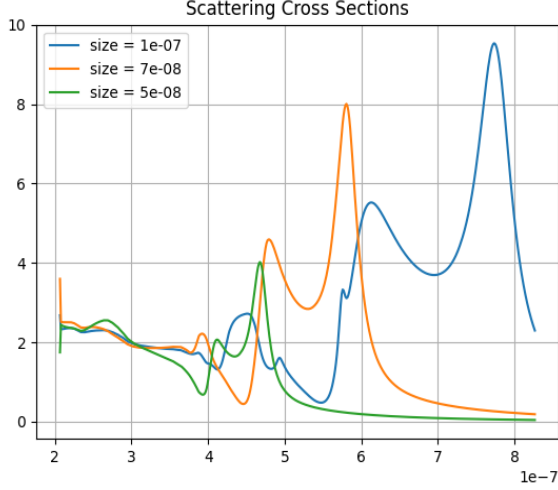


Figure 8: C_{sca} for three different Radius

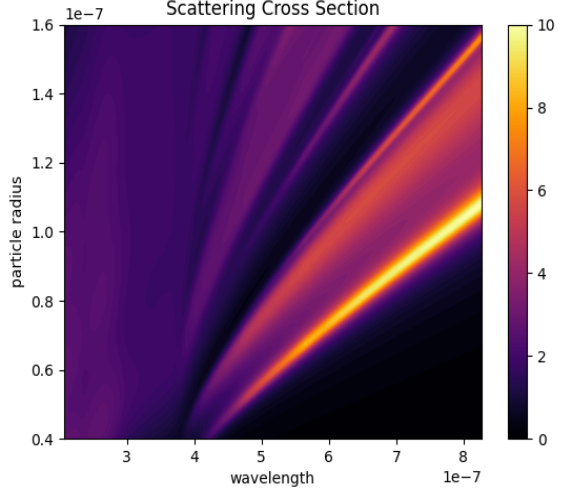


Figure 10: C_{sca} Depending On radius And Wavelength

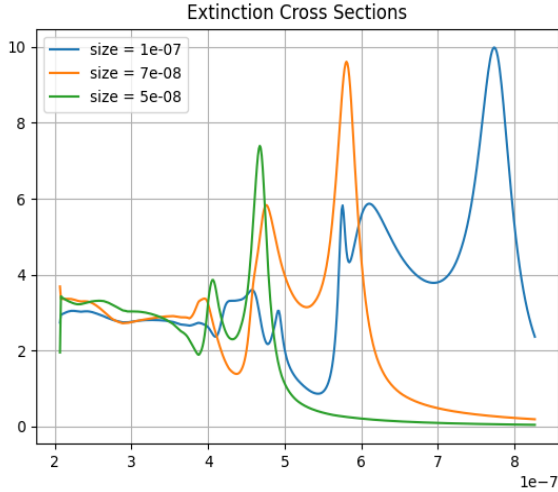


Figure 9: C_{ext} For Three Different Radius

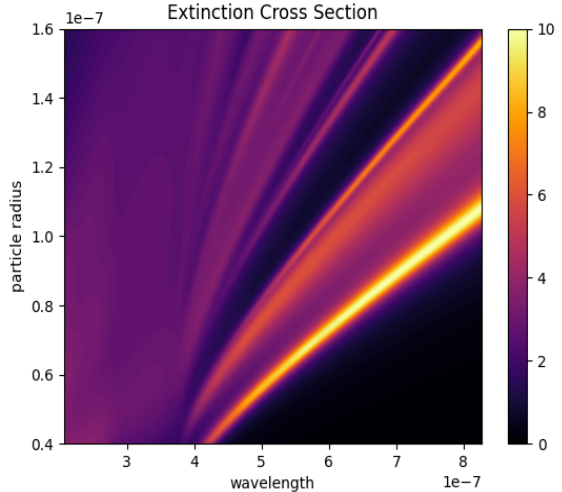


Figure 11: C_{ext} Depending On Radius And Wavelength

rocally. Moreover the scale and the maximum y-value are also decreasing. However, it might be roughly possible to assess that, for our targeted range of values, this shape thus defined is moving left for smaller sizes then right for larger sizes.

If we reproduce our computations with, this time, the radius as a *real* free parameter instead of an arbitrarily fixed value, we obtain the following figures (10) and (11) for the scattering and extinction cross sections respectively. In this way, we can easily visualize our wished *Output* results and compare later with the collected experimental data. It is obvious that, as a really first approximation in our range of values, each maximum and, more particularly, the two global maximum represented by the most intense yellow lines, could be calculated through a linear equation with a different coefficient each explaining, by the way, the compression of the defined shape for smaller radius.

4 Experiments

4.1 Base Description

First, let's describe the procedure to experimentally test and compare our simulation part. Technically, our studied particle should have a spherical shape and the associated material should be *silicon*, as stated in the previous section. Thereby, we are supposed to create a sample composed of spherical nanoparticles of silicon with different sizes included between 100nm and 200nm of diameter. Moreover, in order to approve our theoretical approach and the simulation part, we have to retrieve experimentally an *equivalent shape* made up of the first magnetic and electric dipole modes. In fact, our different sized nanoparticles being randomly scattered on the sample, we have to collect the size of some nanoparticles coupled with the scattering cross section spectrum. In this way, we will be able to link the C_{sca} shape, retrieved thanks to the *optical* microscope, according to the respec-

tive sizes, collected through the *atomic force* microscope, to finally check if it actually fit the simulation.

4.2 Sample Preparation

Chronologically, the first experiment we have to realize is the preparation of the silicon nanoparticle sample.

We have to find a proper support for our different particles. In this way, we use a glass substrate which is composed of a matrix where micrometric number elements are engraved on the top side, in order to see and locate the position of our experiment area on this sample during observation through optical or AFM microscopes. The substrate has the particularity to be transparent which allow the light to cross it and let numbers to be visible as shown on figure (12). Moreover, our goal being to put

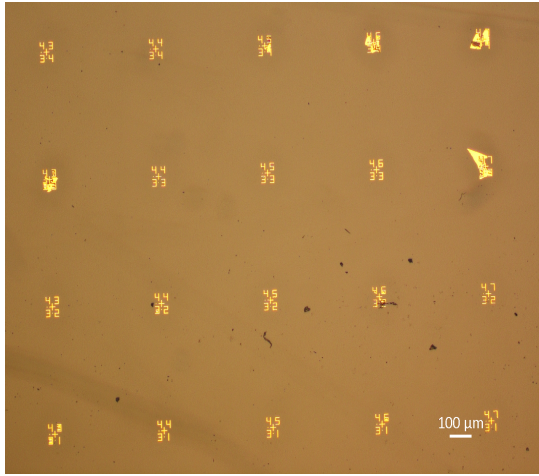


Figure 12: Glass Substrate

nanoparticles on this substrate, we have the following layers described on figure (13).

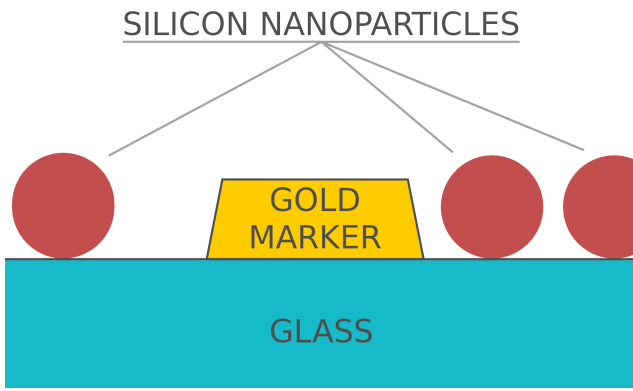


Figure 13: Substrate Layers (Not To Scale)

Secondly, we have to physically produce silicon nanoparticles with *random* sizes included between 50 nm and 100 nm in radius. Hopefully, this step is realized thanks to another research team from the *Kobe University* in Japan. Globally, they are created from SiO lumps annealed at, approximately, 1500°C then etched to produce

Si nanoparticles in a solution. (see [HTM20])

These nanoparticles are placed on the glass substrate pieces thanks to a micropipette: we put a droplet of around 10 microliter on each chip. Afterward, we must either dry in air, or blow dry to progressively remove water from the samples. In the end, our silicon nanoparticles are *dropcasted*.

4.3 Optical Microscope

Now, our goal is to collect the spectrum from some interesting particles, preferably with a large distribution of size starting from 50 nm to 100 nm in radius. In order to select these wished particle and get the equivalent of scattering cross and extinction cross section, we have to use the *optical* microscope. This tool is working like a *basic* microscope, numerically connected to a computer where recorded images might be seen through a normal screen, composed of 3 different objectives and working with 2 different modes of lighting: *bright* and *dark field*. The first one mode is a standard lighting: the ingoing light is emitted from the top part of the *sample area* and the reflecting light is also collected from the top to be transferred to a detector and finally to the computer or directly to the *user-eyes*. The *dark field* is used to in-



Figure 14: Bright Field Example

crease the contrast and avoid the reflected light to be directly collected. Indeed in our case, with the bright mode, all silicon nanoparticles have a narrower range of colors compared to the dark field mode. Thereby, the *dark field* mode allow us to send an incident light and only catch the scattered light as shown on figure (15). It means that only the scattering cross section should be reached for comparison with simulation results. As we can see, the incident direction is described as the edge of a cone and, due to a smaller angle, the scattered light is collected inside the same cone. The figure (16) show an example of our actual sample viewed through the *dark field* mode. Note that the we have a really high contrast and it possible to clearly recognize each color associated to a specific particle or another object.

Then, to collect our wished spectrum, we have to reduce the detected light thanks to a slit. Thereby, only a

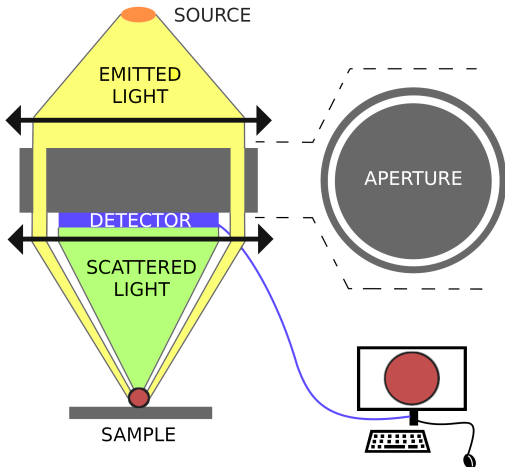


Figure 15: Working Principle Of Dark-Field Optical Spectroscopy

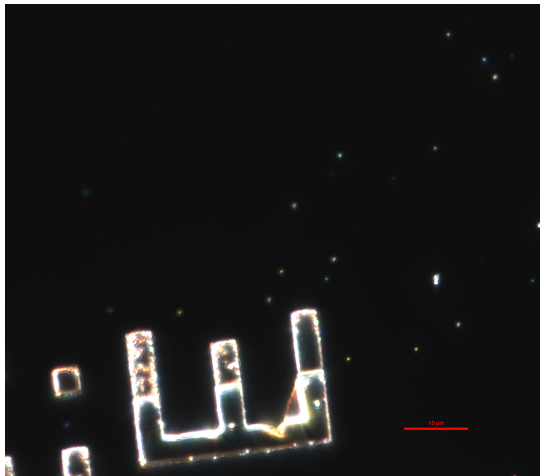


Figure 16: Dark Field Example

few vertical area, with approximately 300 nm of width, should be visible by the detector: the *light noise* created by other particles, horizontally next to our studied nanosphere, is avoided. In fact, the computer software parse each horizontal lines in the *extended-visible* range in order to collect the spectrum of this area: if two particles are on the same line, they will be treated as the same entity. Therefore, that is why we put a narrow aperture to the detector, as shown one the previous figure (17). Also, the function of the spectrometer is to angularly split up the white light source, so that different wavelengths are collected by different pixels of the CCD camera in order to retrieve the wished spectrum.

The first step before actually start our experiment is to calibrate our microscope, that is to say, we have to get some initial data which will be important for computations of the experimental spectrums. In this way, without any incoming light, we save the background spectrum which represents the ambient noise involved by natural emitters like spot lights of the experimental room (which should, ideally, be turned off during the experiments to reduce the noise). We could say that the background

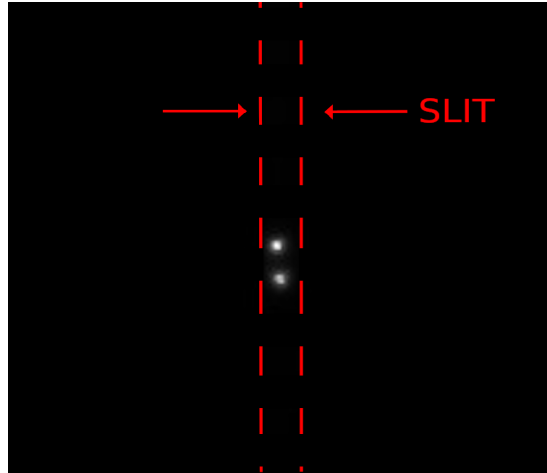


Figure 17: Example Of Slit Closed On Two Particles

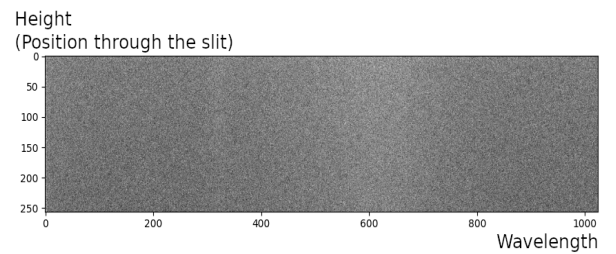


Figure 18: Example Of Background

data are collected on a really specific area because of the slit's thickness, but technically, the stored values are really close and only an average of the noise is relevant in that case.

The incoming light, either in dark or bright field, has a specific distribution because of the halogen light source from *Thorlabs* compagny. Thereby, we put a *reference* object as sample on the microscope's repository: this white material is a diffuse scattering surface which, ideally, scatterers white light uniformly across wavelengths allowing us to retrieve the "Reference spectrum", which includes information about the light source, the optics of the microscope and the spectrometer, as well as the detection efficiency of the CCD camera collecting the light.

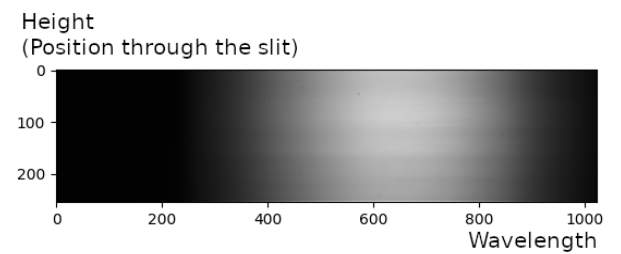


Figure 19: Example Of Reference

The next step is to get the actual spectrum of our wished nanoparticle. Obviously, because of the dimension of the detected area, we get more than one particle on each image. However, with a clever configuration,

we obtain a similar figure from (20) after software computations and treatments. Now, if we extract the line



Figure 20: Raw Data Example

corresponding to our studied particle, we obtain a weird spectrum, pretty close to the following (21). This partic-

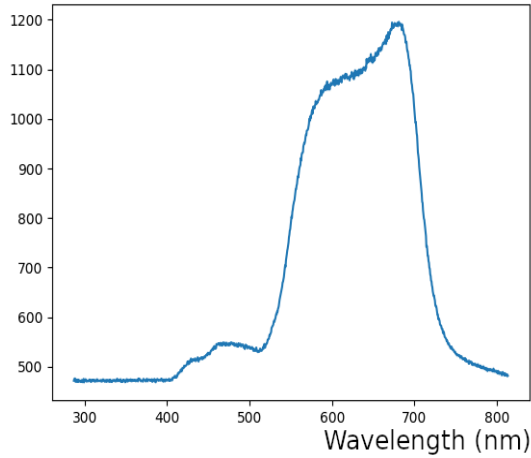


Figure 21: Spectrum From 91 nm Particle Without (4.1) Example

ular shape, very far from our wished simulation results for nanosphere of silicon, is due to the additional *background* and *reference* data. In fact, we have to apply this formula for each pixel.

$$\text{FinalSpectrum} = \frac{\text{RawSpectrum} - \text{Reference}}{\text{Background} - \text{Reference}} \quad (4.1)$$

Note that *Background* is not necessarily a *per pixel* value but could be an average of all pixels stored in *background* as stated previously. Thereby, we obtain the final spectrum, with for instance the figure (22) from the particle in (21). Therefore, this result is much more close to our simulation part with the two first magnetic and electric dipole modes then approximately the same shape shifted along the wavelength axis excepted for all values below, approximately, 450 nm. This last issue is due to the precision of the microscope that is not guaranteed under the visible wavelengths: the light source of the microscope has very low intensity below 400 nm as well as the CCD detector of the spectrometer which has low sensitivity below 400 nm and above 900 nm.

4.4 Atomic Force Microscope

At this point of the experiment part, we have to couple the spectrum, previously retrieved thanks to the optical microscope, with the size of each studied particle.

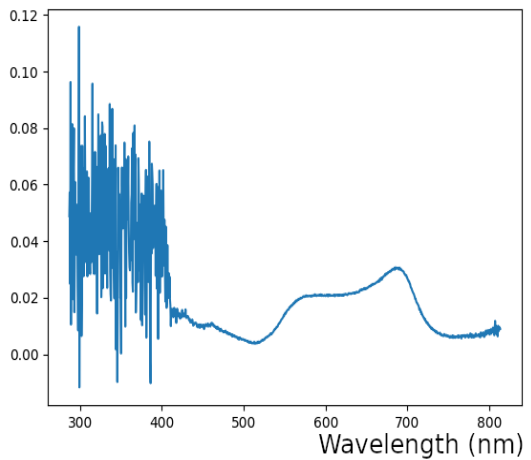


Figure 22: Spectrum From 91 nm Particle With (4.1) Example

Thereby, we need another kind of tool in order to detect physically the wished size, that is to say, an instrument able to measure the diameter, or at least to give an equivalent data, of the desired particle instead of collecting the scattered light intensity. In this way, the best suited tool for this task is the *atomic force microscope*.

The working principle of that kind of microscope is pretty simple. At our *human* scale, the operating mode is roughly similar to the Braille system. Indeed, our sample being totally flat at a macroscopic point of view, the main idea is to drag a tip on the desired experimental surface. This tip is directly connected to a detector collecting the nanometric height variations along the advancement of the last one as shown on figure (23). In this way, if the tip runs into a nanoparticle, it could be possible to subtract the maximum height to the base one, referencing the surface's sample which is the minimum in that case, in order to get the diameter of the particle (assuming that those are spherical).

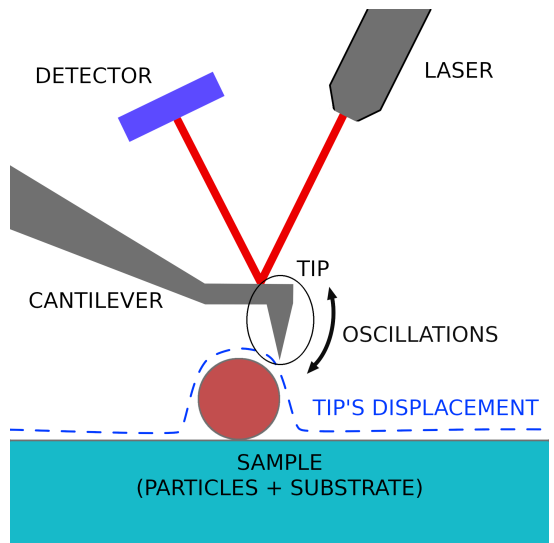


Figure 23: AFM Working Principle

Technically, even if in general an AFM can use differ-

ent methods to scan the sample, in our case, the microscope use the *Van der Waals* forces existing between the tip and the nanoparticles. These forces are responsible of the attraction between different molecules, for instance. Thereby, with no movement, the tip is in balance above the sample without touching it: this is a *non-destructive* scanning tool. The height detector itself is composed of a laser reflecting on the end piece of the cantilever maintaining the tip. When we scan a sample, the tip attached to the cantilever and the laser are moving as a whole block and the tip oscillate around its balance position. In this way, if the tip moves up, compared to its small oscillations, because of a nanoparticle (or another kind of *perturbation*), the optical way runned by the light, and emitted from the laser, is shorter: we detect a height variation. Effectively, the same process happens when the tip moves down. Then, in order to scan a sample, the tip must move along an arbitrary line and, with a pre-defined length, must shift on the next line to reproduce this task until the quantity of line correspond to the length of these last: this procedure is called *raster-scanning*. Afterward, we obtain a square shaped area of our sample. Moreover, multiple scanning modes are available like a double sens scan, that is to say, the tip re-run the scanned line instead of moving out it at the end point, or an horizontal/vertical direction scan, that is to say, the scanned line might be oriented North-South or East-West, and even a start/end point selector, among plenty of other configurations. Additionaly, as the tip is slightly oscillating around its balance position, it is possible to choose the amount of scanned *points* as shown on figure (24), that is to say, the number of periods made compared to the advancement of the system (tip, cantilever and laser) corresponding to the amount of generating pixels for a line. This parameter, associated with the user-defined line's

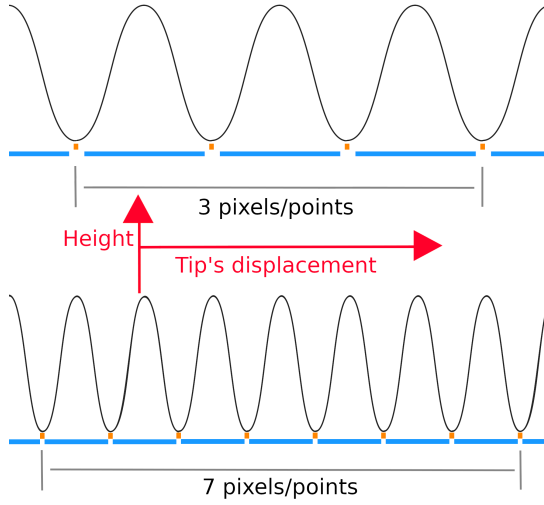


Figure 24: AFM Point Configurations

length, might increase or decrease the quality of the collected data. However, increasing the image resolution increases the scanning time by the same. As a rough idea, to scan a 200×200 nm square with 100 points/pixels takes

around 10 minutes whereas, for a 50×50 nm area with 256 points/pixels takes the same amount of time. Therefore, a precise distribution must be adopted between quality, surface and speed in order to collect enough data and retrieve the nanoparticle's size.

In order to illustrate the whole procedure to retrieve the associated size of our studied particle, we will arbitrarily choose a nanosphere of silicon as shown on figure (25). At first glance, knowing from [Ars+16] that a blue



Figure 25: Example Particle's Image (Dark Field)

scattered light is equivalent to the *smallest* size (~ 50 nm) whereas a red color means the *biggest* one (~ 100 nm), we can easily say that through the yellow-orange color emitted by this particle, we approximate 80 nm of radius. However, we need more precision to check our simulation. Thereby, we use the AFM microscope and execute a scan of the targeted area. Collecting the final data with enough *quality/pixels* to analyse, requires multiple scan in *low quality* and *large dimension* to locate the right particle. Finally, we obtain the following image (26), through the *Gwyddion* software specialized in AFM data analysis, with a resolution of 256 *pixels/points* for the line's width. Note that the scan procedure, started

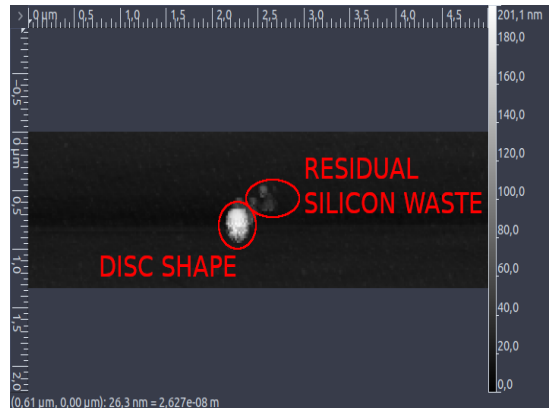


Figure 26: Example Particle's Scan

from the bottom side, was aborted when the particle has entirely been scanned: that is why we observe a rectangular area instead of a squared one. Now, it is much more easier to visualize and get the proper data. As we can

see, the shape of our particle is close to a disc although some residual silicon *waste* on the North-East side. However this image don't reveal the exact diameter, even if we assume a spherical particle, because of the random perturbation on the edge due to the oscillations of the tip when encountering a particle. In this way, the height, being graduated thanks to a grey-scale put on the right, will give us the maximum of the scan. It is already possible to do a hypothesis and approximate the diameter as included between 160 nm and 190 nm. Then, we use a tool from the software, extracting precisely the height scanned along a specific line as shown on figure (27). The

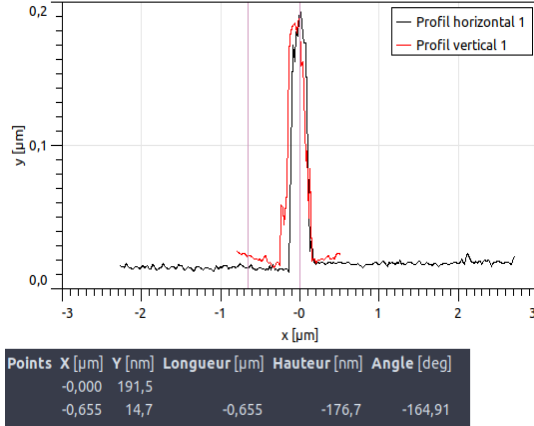


Figure 27: Example Particle's Measurements

extracted pattern was put on the arbitrary defined top of the particle, that is to say the most white part, producing an horizontal and vertical line in black and red respectively. Therefore, we can differentiate the height between the *flat* area and the maximum in order to retrieve the diameter which is, in this case, 176.7 nm giving approximately 88 nm in radius and confirm our first hypothesis.

5 Comparison Between Experiments And Theory

In the end, we are able to confront experiment with simulation results. As a reminder, the procedure is to arbitrarily target a nanoparticle with the optical microscope thanks to numbers sorted into a matrix shape. After getting the associated spectrum, that is to say the scattering cross section depending on the wavelength, we retrieve the associated size through the AFM microscope. This previous diameter is therefore the input for our simulation. Afterward, we compare the experiment's spectrum with the simulated one.

We obtain the following results for a group of particles with their radius included between, roughly, 60 and 90 nm. Note that the experimental curve (purple/pink color) doesn't own the same y-axis than the three others: due to the relation (4.1), unite is not relevant anyway. However, each experimental function has the same scale for all graphs in order to visualize the maximum value increasing while the particle is growing and reciprocally.

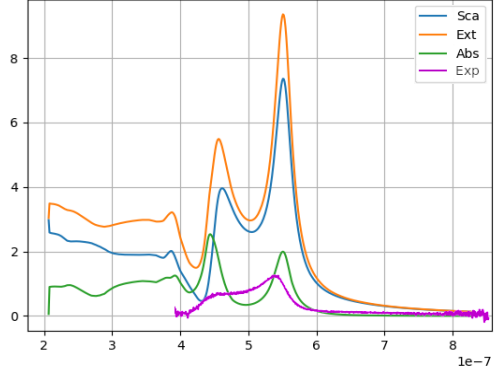


Figure 28: Spectrum For 65 nm (Radius)

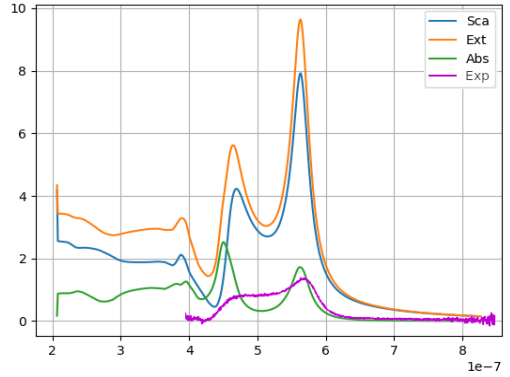


Figure 29: Spectrum For 67 nm (Radius)

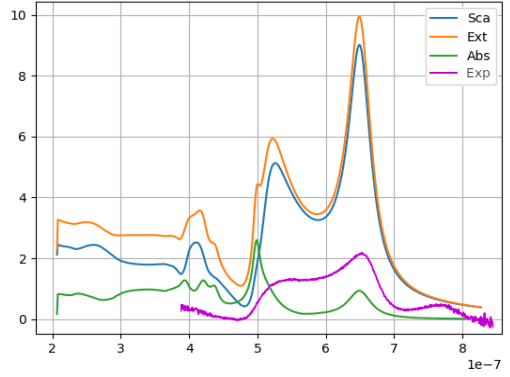


Figure 30: Spectrum For 81 nm (Radius)

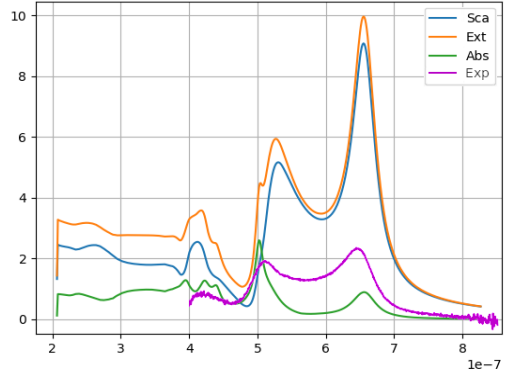


Figure 31: Spectrum For 82 nm (Radius)

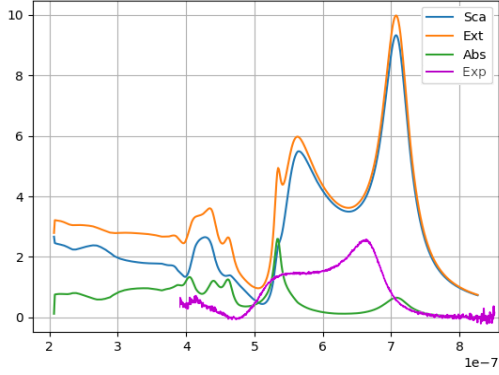


Figure 32: Spectrum For 90 nm (Radius)

As we can see, except for the last one, the two first Mie resonances for both simulated and experienced match the same wavelength positions at approximately 5 nm due to some *human* errors in the retrieved size. However, the 90 nm nanosphere doesn't fit the simulated expectations. A reasonable explanation could be the following: we saw that this particle is relatively close (at 100 nm) to the 81 nm then, due to the smaller size of this last one and some kind of *influences*, the experimental curve is shifted to the left. In the same way, an additional resonance is appearing on the right for the 81 nm particle. Moreover, the proximity of the gold marker and its different refractive index could affect the experimental spectrum.



Figure 33: Relative Positions For Explanation

6 Conclusion

To conclude, thanks to the Mie theory and more precisely, the development of the scattered light for nanoparticles, it is possible to measure, or at least estimate, the associated size of a given nanosphere of silicon by studying the two principal Mie resonances, that is to say evaluate their respective locations and compare with simulations from arbitrary sizes in order to retrieve these maximum on same positions.

7 Acknowledgement

A big thank you to Søren for his patience and his kindness as well as the *Nanomade-Team* including Kirstine, Artyom, Avishek and Mudabar.

References

- [CD83] F. Bohren Craig and R. Huffman Donald. *Absorption and Scattering of Light by Small Particles*. 1983.
- [Lia10] Cai Liang-Wu. “On the computation of spherical Bessel functions of complex arguments”. In: *Elsevier, Computer Physics Communications* (2010).
- [Ars+16] I. Kuznetsov Arseniy et al. “Optically resonant dielectric nanostructures”. In: *American Association for the Advancement of Science, Science* (2016).
- [HTM20] Sugimoto Hiroshi, Okazaki Takuma, and Fujii Minoru. “Mie Resonator Color Inks of Monodispersed and Perfectly Spherical Crystalline Silicon Nanoparticles”. In: *WILEY-VCH Verlag GmbH and Co. KGaA, Advanced Optical Materials* (2020).